Dicle University
Journal of Engineering
https://dergipark.org.tr/tr/pub/dumf
duje.dicle.edu.tr

Research Article

Numerical Evaluation of Failure Modes in Perforated Beams with Hexagonal Openings

Orkun YILMAZ[1*], Yusuf Emir ÖZBAL[2]

[1] Yildiz Technical University, Civil Engineering Department, yilmazo@yildiz.edu.tr, Orcid No: 0000-0001-7457-1242
[2] Yildiz Technical University, Civil Engineering Department, emir.ozbal@std.yildiz.edu.tr, Orcid No: 0009-0007-4690-6675

ARTICLE INFO

Article history:

Received 16 December 2025
Received in revised form 9 June 2026
Accepted 25 June 2026
Available online 10 July 2026

Keywords:

Perforated beam, castellated beam, finite element analysis, Vierendeel bending, web-post buckling

Doi: 10.24012/dumf.1842114

* Corresponding author

ABSTRACT

Steel beams with web openings are widely used due to their high structural efficiency; however, the presence of web openings introduces complex failure modes, such as Vierendeel bending and web-post buckling, which are not observed in solid-web sections. Whereas previous studies have largely focused on opening shape or opening angle, the present study aims to examine whether the failure-mode transition can be interpreted through a more unified geometric proportion. The influence of geometric parameters on the load-bearing behavior and failure mechanisms of perforated beams with hexagonal openings was systematically investigated. Nonlinear finite element analyses were performed on eleven models, comprising a solid-web reference beam and ten constant-depth perforated beams with different combinations of opening angle, opening height, T-section depth, opening spacing, and number of openings. The numerical modeling approach was validated against experimental data from the literature to ensure the reliability of the results. All models were designed with a constant overall depth, allowing the effects of web-opening geometry to be evaluated independently of the depth increase associated with conventional castellated beam fabrication. The analysis results indicate a clear relationship between beam geometry and failure mode. The parameter most closely associated with the transition from ductile, high-capacity flexural failure to brittle, low-capacity shear failure, namely Vierendeel bending, is the dimensionless ratio $2d_t/d_g$, where d_t is the net section depth and d_g is the total beam depth. In the five-opening series, models with higher $2d_t/d_g$ ratios (such as 0.50 and 0.42) reached 86-92% of the capacity of the solid-web beam by developing a ductile flexural mechanism. In contrast, models with a lower $2d_t/d_g$ ratio (0.33) exhibited early brittle failure through the Vierendeel mechanism at 72-79% of the reference capacity. Within the investigated range, the opening angle (θ) showed a comparatively secondary influence. The results suggest that maintaining a higher $2d_t/d_g$ ratio is beneficial for promoting ductile behavior in perforated steel beams and reducing the likelihood of premature Vierendeel failure.

Introduction

Contemporary civil engineering practice is increasingly shaped by the pursuit of material efficiency, economic performance, and sustainability. In this context, the use of steel as a structural material has become more prevalent due to its high strength, ductility, and recyclability. Particularly in the design of industrial facilities, logistics warehouses, multi-story car parks, and large-span commercial buildings, achieving adequate stiffness and load-bearing capacity without increasing structural weight is a significant engineering challenge [1]. However, in many modern applications, designers also face strict architectural constraints, such as limited floor-to-ceiling height (headroom), which restricts the use of deeper structural elements.

Steel beams with web openings are commonly utilized to overcome the aforementioned constraints. In the literature, three principal types of beams with web openings are identified based on fabrication technique and opening geometry. Castellated beams are formed by cutting the web of a standard steel section along a zig-zag pattern and subsequently re-welding the separated halves, resulting in hexagonal openings and an increased overall section depth. Cellular beams are produced through a similar process, but with circular openings introduced during fabrication. Perforated beams of constant depth, on the other hand, are manufactured by directly introducing openings into the web of a standard section, maintaining the original section depth. The use of perforated beams with constant depth is particularly beneficial in applications where headroom is restricted, as this configuration reduces the self-weight of the structure and allows for the integration of building services such as ventilation ducts, piping, and electrical trays within the beam depth. Consequently, the total floor depth is minimized, resulting in a more compact and efficient structural system.

Despite these benefits, beams with web openings exhibit inherent disadvantages. The presence of web openings leads to non-uniform stress distributions that differ significantly from those in solid-web beams. These stress irregularities can cause local concentrations, resulting in failure modes such as web-post buckling or Vierendeel bending [2]. Consequently, the analysis and design of beams with web openings are more complex than those of conventional sections. For this reason, comprehensive numerical and experimental investigations are required to ensure their safe and efficient structural performance.

The fabrication process and the resulting geometry of beams with web openings introduce specific structural vulnerabilities. The web openings reduce the effective shear area, resulting in lower shear capacity compared to solid-web beams. Furthermore, sharp corners in hexagonal openings generate stress concentrations, particularly at the web-flange junctions. These localized stresses can significantly reduce the fatigue life of the beam under cyclic or repeated loading and frequently serve as initiation points for cracks that may propagate through the web over time [3].

Beams with web openings have distinctive structural characteristics that make their design more complex than that of solid-web beams. This complexity arises mainly from their susceptibility to multiple failure modes that either do not occur or manifest differently in solid-web sections. Kerdal and Nethercot [2] developed a core framework to classify these potential failure mechanisms, offering valuable insights into how geometric and load parameters influence structural behavior. Table 1 summarizes the principal failure modes that were identified in their work and are not observed in solid-web beams, along with the key parameters affecting each mechanism. Their study compared analytical predictions with experimental data, finding that while flexural and lateral-torsional failures could be predicted using adapted conventional beam design methods, web-post buckling under compression remains challenging to model precisely. This work established the foundation for understanding and classifying failure modes that are essential in the design and research of castellated beams.

Table 1. Potential failure modes observed in beams with web openings.

Failure Mode	Mechanism
Web-post buckling	Buckling of the vertical web portion (web-post) located between two adjacent openings under combined axial and shear forces.
Vierendeel bending	Formation of local bending moments around the web openings during shear transfer, leading to plastic hinge development in the T-sections.

Zaarour and Redwood [4] carried out an experimental and analytical study on web-post buckling in thin-webbed castellated beams. They tested twelve full-scale specimens and analyzed them using finite element method (FEM) and finite difference method. Their findings showed that web-post buckling is a critical failure mode for slender castellated beams, especially when intermediate plates are used to increase the web depth. The study found that FEM predictions closely align with experimental results, making them a reliable basis for design. In contrast, the simplified graphical method is acceptable but exhibits greater variability.

Redwood and Demirdjian [5] investigated the web-post buckling behavior of castellated beams under shear through both experimental tests and numerical analysis. They tested four full-scale beams and used elastic finite element analyses (FEA) to predict the critical buckling loads. The study found that web-post buckling occurred in all specimens, that the buckling loads were not significantly affected by the moment-to-shear ratio, and that the test loads were 4-14% higher than the FEA predictions. These findings confirm that elastic FEA can effectively estimate the web-post buckling resistance in castellated beams.

Tsavdaridis and D'Mello [6] conducted an extensive nonlinear FEA of perforated steel beams to examine the Vierendeel bending mechanism across various web-opening shapes, including both standard and innovative types. Their comparison of eleven different opening geometries focused on how these shapes influence shear-moment interaction, plastic hinge development, and stress distribution. They discovered that elliptical openings provide better stress distribution and higher combined shear capacity than circular or hexagonal openings, leading to a recommendation to use elliptical openings to enhance structural performance and design efficiency.

Budi et al. [7] carried out an experimental and numerical investigation to optimize the hexagonal opening angle and spacing in castellated steel beams. Validated by experimental tests, the study examined sixty models, varying the opening angle from 45° to 70° and the web-post distance (e) over a broad range ($0.042h_o$ to $3.153h_o$). The findings showed that the optimal configuration was with a 60° opening angle and a web-post distance (e) between $0.186h_o$ and $0.266h_o$. Additionally, the research revealed that the point of maximum stress concentration shifts from the corner of the hole (for wider spacing) to the web-post weld joint (for shorter spacing).

Ponsorn and Phuvoravan [8] performed a detailed analytical study to assess the structural performance of castellated and cellular beams based on the AISC Design Guide 31. They examined key design modes, geometric constraints, and beam span lengths to create efficiency charts and practical design guidelines. The results showed that castellated beams generally have higher efficiency than cellular beams, especially across a wider range of spans. Cellular beams become efficient primarily when their length exceeds about 30 times their radius of gyration. The opening cut angle was reported to have only a minor effect on efficiency compared with the web-post width and the span, which provides an early indication that the opening angle acts as a secondary parameter.

Barkiah and Darmawan [9] conducted a numerical study to compare the flexural performance of standard steel beams and castellated beams with different hexagonal opening angles. Their findings revealed that web openings enhance bending capacity by about 8-19% relative to solid-web beams. The best flexural performance occurred with opening angles between 45° and 50°, while increasing the angle to 60° reduced capacity, suggesting that an opening angle too large can weaken the section. Notably, this optimal angle range differs from the 60° value reported by Budi et al. [7]. This inconsistency across studies indicates that the opening angle, when considered in isolation, is not a reliable predictor of structural behavior.

Ferreira et al. [10] examined the web-post buckling resistance of perforated steel beams with elliptical web openings using FEA and parametric studies in accordance with Eurocode 3 (EC3) guidelines. They analyzed 5400 geometric models to understand how the opening height, web-post width, web thickness, and opening shape influence shear buckling capacity. The researchers created and validated a new design method compatible with EC3 that accurately forecasts web-post buckling resistance. Their findings show that smaller expansion ratios and lower opening heights notably enhance capacity, and the results align well with detailed FE simulations.

More recent studies have further clarified the role of opening ratio and web-post width in beams with web openings. Morkhade and Gupta [11] observed that when the opening ratio exceeds 0.75, both the stability and strength of perforated beams are significantly reduced. In contrast, opening ratios less than 0.5 have a limited impact on overall performance. In related work, Morkhade et al. [12] conducted experimental and numerical investigations and found that web-post width is a critical parameter for strength capacity. Specifically, narrow web-posts result in substantial strength reduction and web-post buckling, while increasing the web-post width leads to notable improvements in performance.

The effect of opening shape has been examined in several recent numerical studies. Khan et al. [13] investigated five different opening shapes and reported that increasing web-post width consistently enhances capacity across all configurations. Among the shapes considered, hexagonal openings achieved the highest ultimate load, while square openings resulted in the lowest, and circular openings exhibited the smallest ultimate deflections. Patil and Kumbhar [14], in their study of castellated beams with increased depth, found that diamond-shaped openings provide superior load-carrying capacity and reduced deflection compared to hexagonal and circular alternatives. Similarly, De'nan et al. [15] evaluated corrugated-perforated sections and concluded that larger openings decrease performance, with diamond-shaped perforations outperforming square ones. Hashim and De'nan [16] reported that the use of a c-hexagon opening, combined with an optimized opening layout, can reduce displacement compared to other patterns. This result highlights the sensitivity of local stress concentration and load-transfer mechanisms to geometric detailing. Promsatit et al. [17] further demonstrated that elliptical openings, when properly proportioned and spaced, enhance web-post buckling resistance relative to circular openings, emphasizing the importance of geometric proportioning in design. The same study also reported that a higher opening-height-to-depth ratio reduces the web-post buckling resistance by decreasing the depth of the T-section, which links the resistance of the section directly to the proportion of the overall depth occupied by the opening.

Recent investigations have contributed to a better understanding of both local and global instability phenomena in beams with web openings. Sae-Long et al. [18, 19] found that web-post horizontal moment and horizontal shear in cellular beams are significantly affected by opening ratio, slenderness ratio, and section size. Their results indicate that design expressions based on AISC provisions may overestimate local resistance in these cases. Betken et al. [20] and Bhat et al. [21] also noted that while castellated beams can achieve higher flexural efficiency compared to solid sections, they are more susceptible to lateral-torsional buckling and combined local-global instability, primarily due to increased depth and reduced torsional rigidity.

In summary, the recent literature demonstrates that the structural response of beams with web openings is governed by the combined effects of opening shape, size, spacing, web-post width, and overall member stability. It should be noted that most existing studies have concentrated on conventional castellated or cellular beams, which typically involve an increase in overall depth during fabrication, or have examined alternative opening shapes rather than the constant-depth hexagonal configuration addressed in the present work. In particular, the governing geometric variables have largely been examined in isolation, and a unified geometric ratio that can consistently indicate the transition between failure modes has not been sufficiently established. As a result, although prior research has identified key failure modes and controlling parameters, further study is required to clarify the influence of geometric variables on the in-plane behavior of constant-depth perforated beams.

In this study, constant-depth perforated steel beams were examined by introducing hexagonal openings directly into the web of a solid-web section. This approach allows the effects of opening geometry to be investigated without increasing the overall section depth. Therefore, the present work differs from conventional castellated beam studies, in which depth increase and opening geometry are coupled. Nonlinear FE models were developed using Ansys Workbench [22], and the modeling methodology was verified through comparison with experimental data available in the literature [23]. The FE models were constrained to in-plane response by restraining out-of-plane displacements and lateral-torsional buckling, thereby simulating laterally supported conditions. This modeling strategy enables the assessment of the influence of geometric proportions on the transition between failure modes. The primary aim of the study is to identify a geometric parameter associated with the transition from ductile flexural behavior to premature shear-related mechanisms, such as Vierendeel bending or web-post buckling. Based on this interpretation, the study also provides initial recommendations for proportioning constant-depth perforated beams toward more ductile behavior.

Finite element models

Geometric properties

This study conducted FE analyses on ten perforated beam models featuring hexagonal openings with varied numbers, angles, and sizes, along with a solid-web reference beam for comparison. The analysis considered geometric parameters such as the edge length or spacing (e), the horizontal projection of the opening slope (b), the depth of the T-section (d_t), and the opening height (h_o). All geometric properties of the beam models are shown in Figure 1. Each beam has a 5.0 m span, a total depth (d_g) of 600 mm, flange thickness (t_f) of 12 mm, web thickness (t_w) of 8 mm, and flange width (b_f) of 200 mm. The dimensions, total mass, and normalized mass ratios of the perforated beams are summarized in Table 2. The naming convention reflects the opening angle (θ) and the number of openings in the web; for example, in model A40-5, "40" denotes the hexagonal opening angle θ, and "5" indicates the total number of openings along the beam.

As indicated in Table 2, the introduction of web openings leads to a significant reduction in the total mass of the beam. The solid-web reference beam has a mass of 369.26 kg, whereas the perforated beam models have masses ranging from 305.87 kg to 338.35 kg. The normalized mass ratios are between 82.83% and 91.63%, corresponding to a maximum weight reduction of 17% as a result of the web openings. In terms of the plastic section modulus about the major axis (W_{px}), a decrease of approximately 8.66% to 15.41% is observed compared to the solid-web reference beam.

It should be noted that the parametric matrix used in this study is not fully orthogonal, since the opening angle, opening height, T-section depth, and number of openings are varied simultaneously across the model set. As a result, the influence of each variable cannot be entirely isolated, and the reported trends should be interpreted with respect to the investigated parameter ranges.

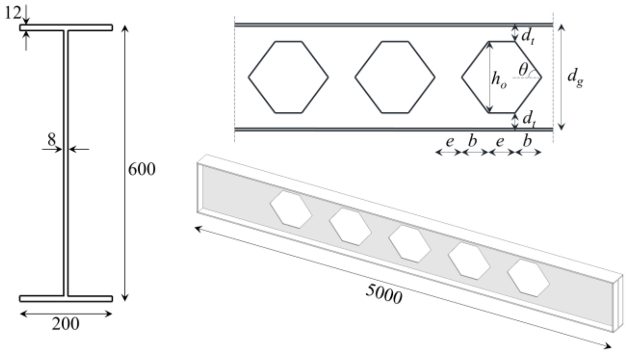

Figure 1. Geometric properties of the perforated beams used in the study (units: mm).

Boundary conditions and loading scheme

The beams examined in this study were modeled with simply supported boundary conditions. One end restricted the displacements in all three directions (U_x, U_y, and U_z), while allowing rotational freedom. This setup aligns with the typical simple support described in the literature. Conversely, at the other end, the beam could translate along its longitudinal axis, with displacements in the other two directions restricted and rotations free. This arrangement simulates a simple roller support, permitting axial expansion or contraction under load without additional restraint forces.

In the FE models, out-of-plane displacements along the top flange were fully restrained to prevent the occurrence of lateral-torsional buckling in the beams. By applying this boundary condition, the structural response was mainly governed by the presence and configuration of the web openings under the adopted assumptions, thereby suppressing global instability effects. The continuous restraint applied to the top flange simulates the lateral support typically provided in building structures by a floor slab, either composite or non-composite, acting as a diaphragm, or by closely spaced secondary beams.

Loading was implemented as a displacement-controlled load at the midpoint of the top flange. During analysis, incremental displacements were applied, and the resulting reaction forces were recorded to create load-displacement curves.

Table 2. Geometric parameters and mass values of the analyzed beams

Beam	e (mm)	b (mm)	h_o (mm)	d_t (mm)	θ (°)	Mass (kg)	Normalized mass (%)	A_n (cm^2)	W_{px} (cm^3)
A40-5	150	178.2	300	150	40	338.35	91.63	70.08	1894.75
A40-7	150	178.2	300	150	40	325.99	88.29	70.08	1894.75
A45-5	200	200	400	100	45	319.02	86.39	62.08	1754.75
A45-6	200	200	400	100	45	308.98	83.68	62.08	1754.75
A52-5	200	156.3	400	100	52	324.52	87.88	62.08	1754.75
A52-7	200	156.3	400	100	52	306.62	83.04	62.08	1754.75
A60-5	200	115.5	400	100	60	329.64	89.27	62.08	1754.75
A60-8	200	115.5	400	100	60	305.87	82.83	62.08	1754.75
A63-5	200	89.2	350	125	63	337.48	91.39	66.08	1829.76
A63-8	200	89.2	350	125	63	318.42	86.23	66.08	1829.76
Solid-web	-	-	-	-	-	369.26	100	94.08	2074.46

In the FE models, geometric nonlinearity was considered by activating the large-deflection option in Ansys Workbench. The analysis was carried out on the deformed geometry, and the structural stiffness was updated incrementally throughout the loading process. This approach enabled the model to capture the reduction in stiffness and the redistribution of nonlinear stresses in the vicinity of the web openings. Since lateral-torsional buckling was intentionally prevented, the geometric nonlinearity in this study was mainly used to simulate the local nonlinear deformation behavior near the web openings.

Material properties

In the analysis, S355 structural steel was used, a common material in steel construction. Its density is 7850 kg/m^3. The steel was assumed to be isotropic, with an elastic modulus (E) of 200,000 MPa and Poisson's ratio (v) of 0.3.

A bilinear isotropic hardening model was adopted to simulate the nonlinear behavior of steel. In this model, the material exhibits plastic deformation with a defined strain-hardening slope following yield. The yield stress (F_y) was specified as 355 MPa, and the tangent modulus (E_t) was set to 2000 MPa, corresponding to 1% of the elastic modulus.

The material model employed in this study does not include a damage or fracture criterion. Therefore, the analyses are limited to capturing the initiation and progression of primary failure mechanisms such as yielding, plastic hinge formation, and web-post buckling, without representing material rupture or crack propagation. This modeling approach is appropriate for the in-plane, geometry-dependent comparisons that constitute the main objective of the present investigation.

Mesh structure

Figure 2 illustrates an example of the mesh structure used in the perforated beam models developed in this study. The mesh was created using the SOLID186 element, a widely used three-dimensional solid element in Ansys FE software. This hexahedral (brick) element is a high-order type, offering enhanced accuracy in nonlinear analysis. Each SOLID186 element features 20 nodes, with three degrees of freedom at each node: translations along the x, y, and z axes [24]. Its higher-order shape functions improve precision in nonlinear simulations, especially for modeling parts with complex stress patterns and localized stress concentrations. As a result, the SOLID186 element is well-suited for simulating perforated beams, where such effects are likely to occur in the web region.

A uniform and fine mesh density was applied throughout the beam models in this study. This approach ensured that regions around the openings, as well as the flange and web sections, were discretized with small, consistent elements. Consequently, the mesh was intended to capture stress concentrations near the corners of the hexagonal openings and in narrow cross-sectional areas without additional local refinement. Additionally, multiple element layers were used through the thickness of the web and flanges to improve the representation of stress distributions arising from shear and bending effects.

The adopted mesh contained approximately 35,000-38,000 elements in the perforated beam models, with an average element size of approximately 15 mm in the web-opening region and two and three element layers through the web and flange thickness, respectively.

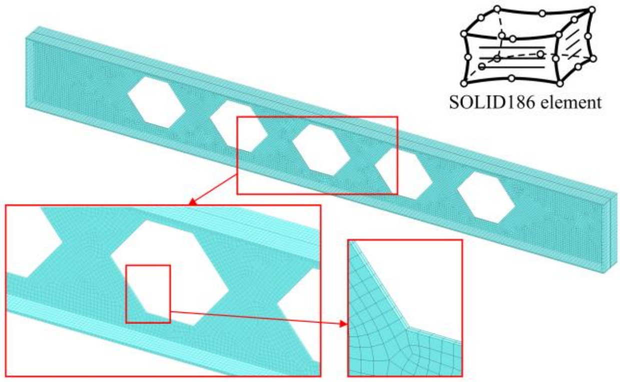

Figure 2. Example of the FE mesh on the perforated beam model and schematic representation of the SOLID186 element.

Finite element model validation

To demonstrate the accuracy and reliability of the nonlinear FE modeling strategy employed in this study, a validation analysis was performed by replicating a full-scale experimental test from the literature. An experimental study by Tsavdaridis and D'Mello [23] investigating the web-post buckling behavior of perforated steel beams was selected as the benchmark. Specifically, the cellular beam specimen designated as "Specimen A1", fabricated from a UB 457×152×52 section, was modeled using the same element type (SOLID186) and boundary conditions as described in the previous sections. The mesh strategy described in the previous section was established for the perforated beam models and applied consistently to the validation model. This strategy involved a fine and uniform mesh in the web-opening region, and multiple element layers through the web and flange thicknesses. The geometric dimensions and the FE mesh configuration are shown in Figure 3.

Specimen A1 is a cellular beam with circular web openings and therefore differs in opening geometry from the hexagonal perforated beams investigated in the present study. However, the purpose of the validation is not to reproduce a specific opening shape, but to assess the FE modeling methodology, including the element formulation, material constitutive model, nonlinear solution procedure, and mesh strategy. In addition, web-post buckling, which was observed as the failure mode in Specimen A1, is also a critical failure mechanism in beams with hexagonal web openings. Therefore, Specimen A1 is considered suitable for validating the FE modeling approach adopted in this study.

The material properties for the validation model were defined based on the modeling approach presented in the reference study [23]. In their work, they compared numerical results using two different material definitions: "FEM 1", which utilized actual material properties obtained from tensile coupon tests, and "FEM 2", which adopted nominal design values for S355 grade steel. For the present validation analysis, the material parameters corresponding to the "FEM 2" model were adopted to ensure consistency with standard design assumptions. Accordingly, the yield strength (F_y) was defined as 355 MPa, and the tangent modulus (E_t) was assumed to be 580 MPa, as indicated in the reference study [23].

The comparison between the numerical and experimental load-displacement curves is presented in Figure 4. As shown, the FE model agrees well with the experimental data in terms of initial stiffness within the elastic region. Notably, during the yielding phase, the numerical curve closely follows the trajectory of the "FEM 2" model in the reference study [23], consistent with the use of identical nominal material properties. While the ultimate load capacity predicted by the present FE model (320 kN) is approximately 10% higher than the experimental value (~290 kN), the model reasonably reproduces the post-peak trend, where the stability loss trend converges back towards the experimental curve. The difference in peak load is attributed to the idealized nature of the FE model, which assumes a homogeneous material and excludes the residual stresses inherent in the physical specimen that typically cause gradual yielding and reduced capacity. Given that the reference numerical model (FEM 2) also predicted a higher capacity, the current results are considered acceptable for nonlinear stability analyses.

The numerical curves reported by Tsavdaridis and D'Mello [23] for FEM 1 and FEM 2 differ from the present model mainly in terms of peak load and post-peak response. The reference FEM curves reach higher peak loads, whereas the present solid-element model predicts a lower peak load and a smoother post-peak degradation trend. These differences may be attributed to differences in element formulation, mesh representation, and initial imperfection assumptions. The reference study employed four-node linear shell elements and introduced geometric imperfections with an amplitude of $t_w/200$, while the present model uses twenty-node solid elements without explicitly introduced geometric imperfections. Therefore, the present model is not intended to reproduce the reference FEM curves point by point, but to provide a consistent nonlinear modeling framework for the comparative analyses in this study. A solid-element re-analysis of the same specimen by Promsatit et al. [17] produced a similar response, indicating that the observed differences are consistent with the adopted modeling formulation.

Furthermore, a qualitative comparison of the failure modes is provided in Figure 5. The equivalent plastic strain distribution obtained from the FE model (Figure 5a) shows good agreement with the failure mechanism observed in the experimental test (Figure 5b). Both the experiment and the numerical simulation indicate that the failure is governed by the web-post buckling mode, characterized by the out-of-plane twisting of the web section between the openings.

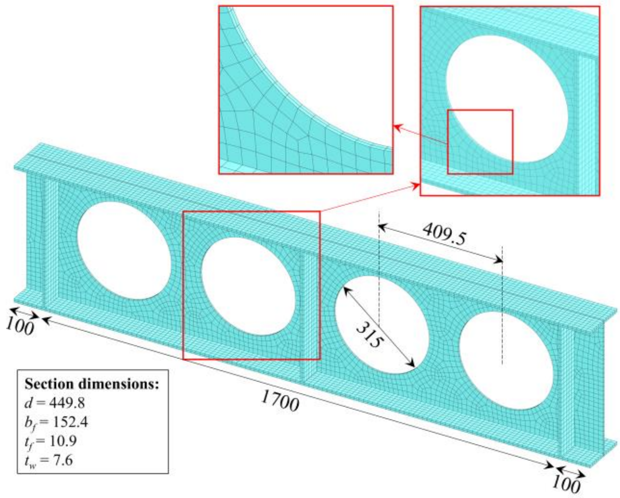

Figure 3. The geometric dimensions and the finite element mesh configuration of FE model of "Specimen A1" tested by Tsavdaridis and D'Mello [23]

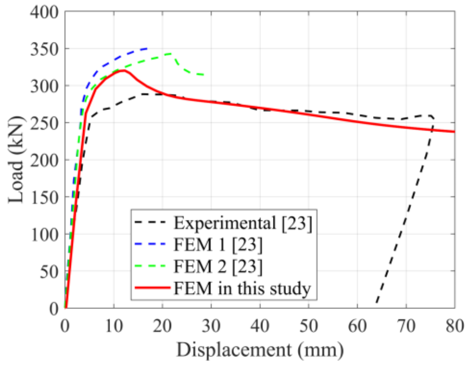

Figure 4. Comparison of experimental and numerical load-displacement curves reported in the reference study [23] with the FEM result obtained in the present study.

In summary, the close agreement in stiffness, failure mechanism, and ultimate load capacity demonstrates that the FE modeling approach employed in this study is capable of reasonably reproducing the in-plane response and failure mechanism relevant to the comparative analyses. Although a separate mesh convergence study was not performed for the parametric models, the same discretization strategy was used consistently throughout the validation and parametric analyses.

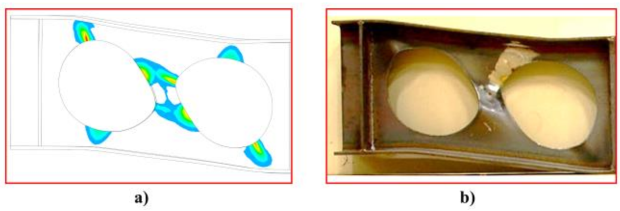

Figure 5. Comparison of failure modes: (a) Numerical equivalent plastic strain distribution; (b) Experimental web-post buckling [23]

Analysis results and discussion

Nonlinear FE analyses were performed to investigate the structural behavior of ten perforated beam models and a solid-web reference beam. For each model, the load-carrying capacity was taken as the peak of the load-displacement curve. The associated failure mode was identified from the shape of the curve, the post-peak response, the plastic strain distribution, and the design-code checks, rather than from the termination point of the analysis.

Load-displacement curves and capacity comparisons

The load-displacement curves depict the relationship between mid-span vertical displacement and the reaction force, offering insights into the overall structural behavior. The study compared perforated beams with five different opening angles (40°, 45°, 52°, 60°, and 63°), each with two variations in the number of openings, against the solid-web reference beam, as shown in Figure 6. Furthermore, for each beam, the maximum load, initial stiffness, and normalized load values relative to the solid-web beam are summarized in Table 3.

As shown in Figure 6, the solid-web reference beam attained a peak load of 1210.50 kN and exhibited pronounced ductile behavior under loading. As expected, all perforated beam models with web openings demonstrated lower initial stiffness and reduced maximum load capacity compared to the solid-web beam. However, significant variation was observed among the perforated models. In particular, models A40-5 and A63-5 achieved the highest performance, reaching 92.34% and 86.66% of the capacity of the solid-web beam, respectively, and their load-displacement curves indicated a ductile response similar to the reference beam. In contrast, the lowest capacities were obtained for models A60-8 and A52-7, at 56.05% and 57.15% of the capacity of the solid-web beam, respectively. Notably, these lower-performing models exhibited a sudden drop in load immediately after reaching peak load, which is suggestive of a brittle failure mechanism rather than a ductile collapse.

Effects of geometric parameters and failure modes

The plastic strain distributions highlight regions where the material surpasses its elastic limit, leading to permanent deformation. These visuals help illustrate how each beam model responds to loading conditions. The plastic strain distributions for the perforated beam models are shown in Figures 7-11, while the distribution for the solid-web beam model is displayed in Figure 12. Figures 7-11 are presented using a common equivalent plastic strain scale to allow direct comparison among the perforated beam models. Figure 12 is plotted with an independent scale because the plastic strain level in the solid-web beam is considerably lower; using the same scale would obscure the mid-span plasticization pattern.

As anticipated, plastic strain in the solid-web reference beam was concentrated at the mid-span, corresponding to the location of maximum bending moment. This distribution indicates that the beam developed a flexural plastic mechanism consistent with ductile flexural behavior.

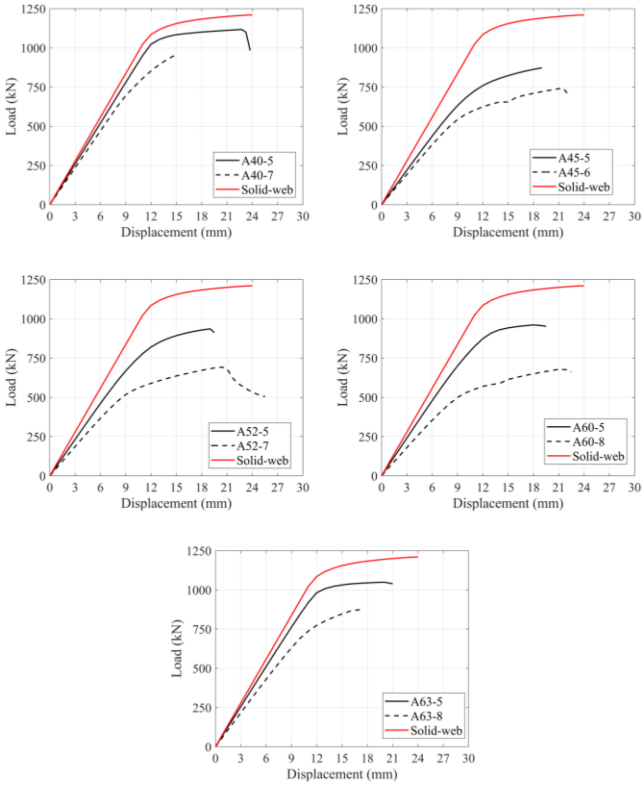

Figure 6. The load-displacement curves of the perforated beams and the solid-web reference beam.

Table 3. Maximum load, initial stiffness, and normalized load values for each perforated beam compared to the solid-web reference beam.

Beam	Maximum load (kN)	Initial stiffness (kN/mm)	Normalized load (%)
A40-5	1117.80	86.69	92.34
A40-7	957.78	78.56	79.12
A45-5	873.28	73.29	72.14
A45-6	743.68	64.27	61.44
A52-5	936.11	77.16	77.35
A52-7	691.82	61.72	57.15
A60-5	961.25	80.15	79.41
A60-8	678.48	59.61	56.05
A63-5	1049.00	85.34	86.66
A63-8	873.68	71.99	72.18
Solid-web	1210.50	93.08	100

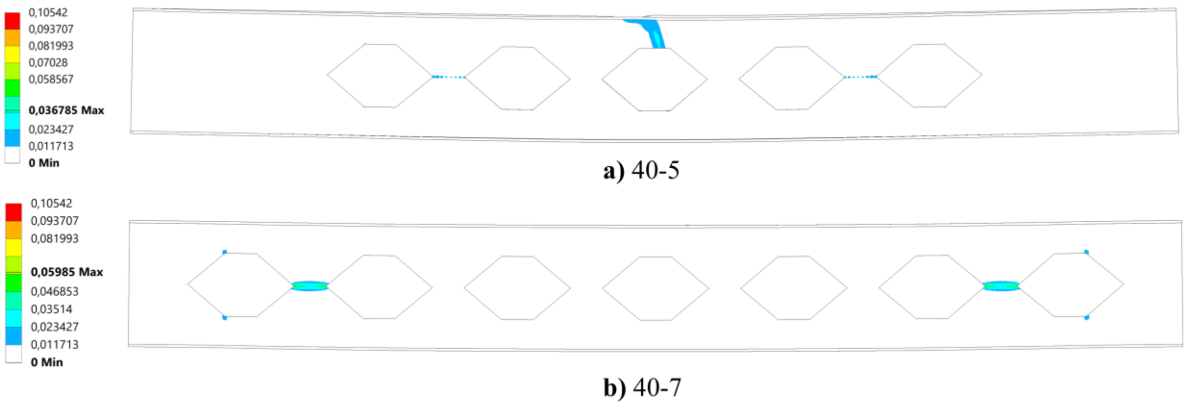

Figure 7. Plastic strain distributions of the perforated beams with a 40° opening angle.

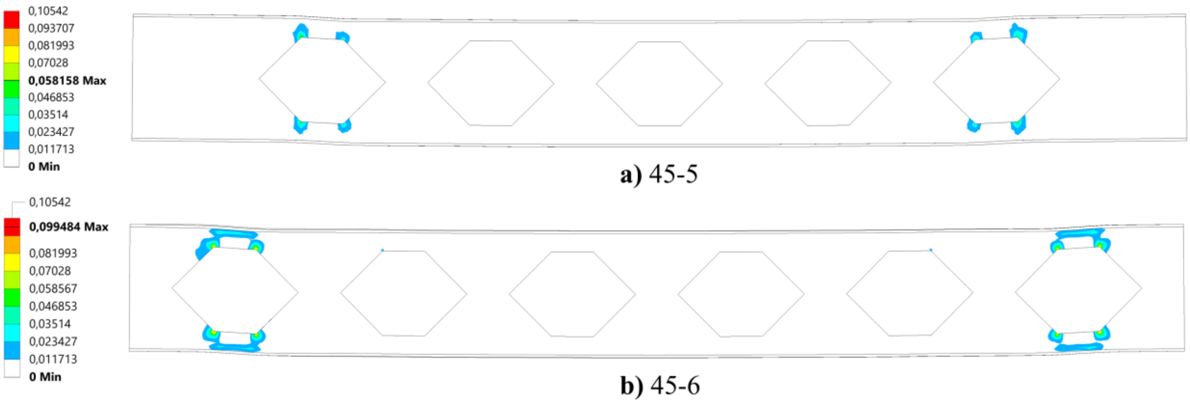

Figure 8. Plastic strain distributions of the perforated beams with a 45° opening angle.

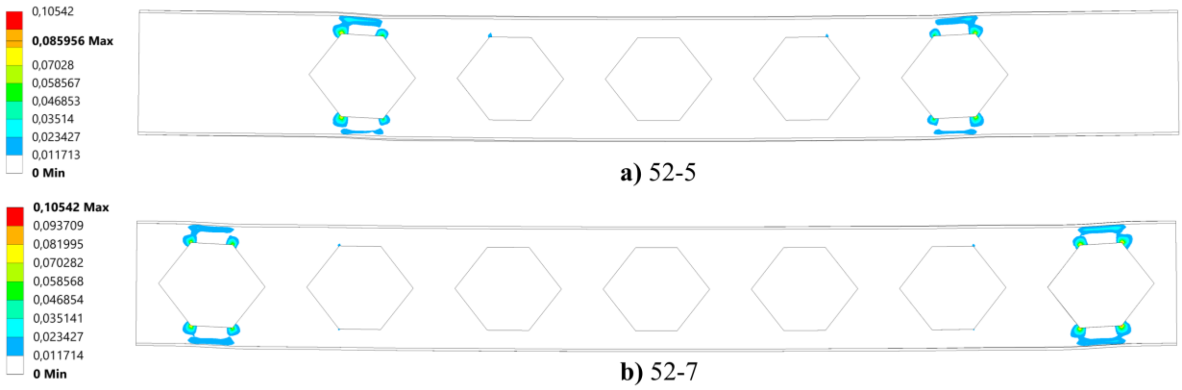

Figure 9. Plastic strain distributions of the perforated beams with a 52° opening angle.

The failure modes observed in the perforated beams deviated from the ideal behavior of the solid-web reference. In the A40-5 and A63-5 models, which exhibited the highest load capacities, plasticization was concentrated near the mid-span, corresponding to the region of maximum bending moment, similar to the reference beam. This result indicates that the opening geometry in these models provided sufficient resistance to shear forces and local effects, allowing the beams to develop a ductile flexural failure mechanism comparable to that of the solid-web beam.

In contrast, the A45-5, A45-6, A52-5, A52-7, A60-5, A60-8, and A63-8 beam models exhibited different failure mechanisms. In these cases, plastic strains were primarily concentrated near the corners of the outermost openings, adjacent to the supports where shear forces are predominant. This pattern is indicative of a classic Vierendeel mechanism, in which local bending moments generated during shear transfer around the openings exceed the capacity of the T-sections. As a result, these beams experienced localized plastic deformation prior to developing a global flexural mechanism, which explains their reduced load capacity and brittle post-peak response.

The observed difference in the location of plastic strain provides a useful indication of the transition between failure modes. Plastic strain concentration around the opening

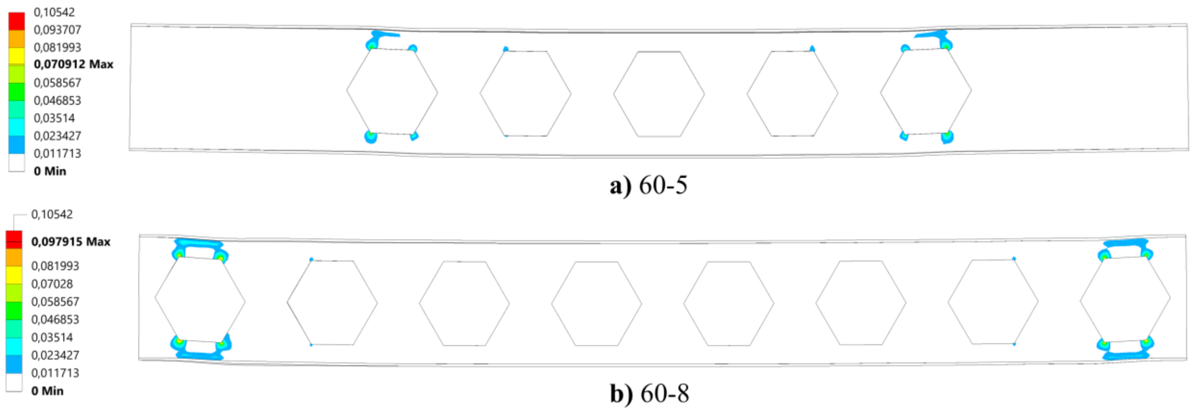

Figure 10. Plastic strain distributions of the perforated beams with a 60° opening angle.

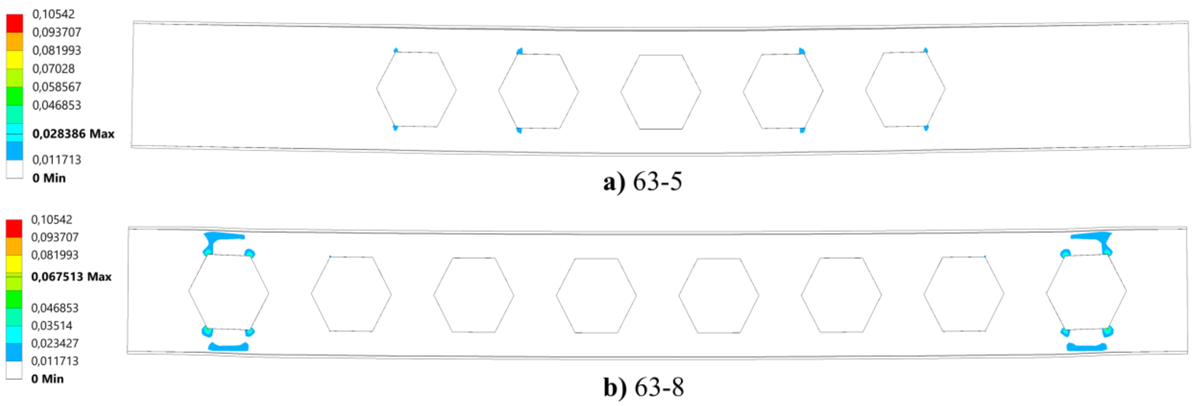

Figure 11. Plastic strain distributions of the perforated beams with a 63° opening angle.

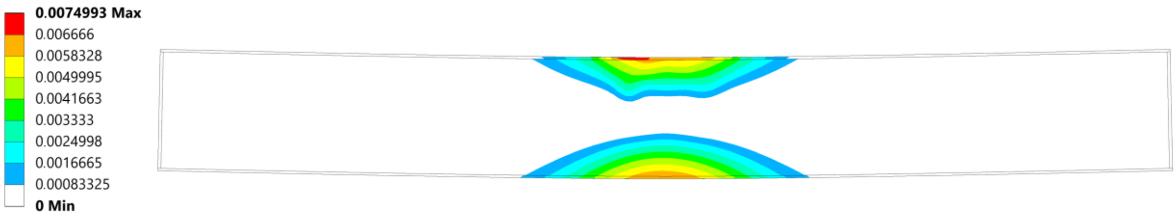

Figure 12. Plastic strain distributions of the solid-web beam.

edges indicates a local mechanism governed by Vierendeel bending. In contrast, the mid-span plastic strain pattern observed in models A40-5 and A63-5 is associated with a global flexural mechanism, in which plasticity develops primarily in the high-moment region rather than around the web openings. The mechanical basis for this transition is quantitatively evaluated in the subsequent subsection.

Additionally, in the A40-7 beam model, a high concentration of plastic strains was observed in the horizontal web-post region between adjacent openings, indicating a web-post-dominated failure mode rather than a Vierendeel mechanism.

At first glance, variations in beam performance with different opening angles may appear to be primarily governed by the angle parameter. However, in addition to the opening angle and the number of openings, other geometric characteristics, such as opening height (h_o), the horizontal projection of the opening slope (b), the edge length of the hexagon or spacing between openings (e), and the depth of the T-section (d_t), also differ among the models. Therefore, it is evident that the load-carrying capacity is influenced not only by the opening angle but also by the combined effects of multiple geometric parameters. To provide a more comprehensive evaluation, a set of dimensionless geometric ratios was calculated for the beam models with five openings, as presented in Table 4.

Table 4. Dimensionless geometric ratios of five-opening models and normalized load values relative to the solid-web beam

Beam	h_o/d_g	$2d_t/d_g$	b/h_o	e/h_o
A40-5	0.50	0.50	0.59	0.50
A45-5	0.67	0.33	0.50	0.50
A52-5	0.67	0.33	0.39	0.50
A60-5	0.67	0.33	0.28	0.50
A63-5	0.58	0.42	0.25	0.57

As indicated in Table 4, the ratio of the total T-section depth to the overall beam depth ($2d_t/d_g$) appears to be the geometric factor most closely associated with whether the observed response is dominated by a global flexural mechanism, Vierendeel bending, or web-post buckling. Beams that demonstrated ductile failure, such as A40-5 and A63-5, had the highest $2d_t/d_g$ ratios of 0.50 and 0.42, respectively. These deeper T-sections provide greater resistance to Vierendeel effects, allowing the beams to approach their flexural capacity. In contrast, beams that exhibited Vierendeel-type failure (A45-5, A52-5, and A60-5) had a lower $2d_t/d_g$ ratio of 0.33. This observation indicates that the relatively high capacity of the A40-5 model appears to be more closely associated with its greater T-section depth than with the 40° opening angle alone.

For the A45-5, A52-5, and A60-5 beam models, which share a constant $2d_t/d_g$ ratio of 0.33, the b/h_o ratio appears to have a secondary influence on performance. As the horizontal length of the opening slope (b) decreases (from A45-5 to A60-5, resulting in a reduction of the b/h_o ratio from 0.50 to 0.28) while the opening height (h_o) remains constant, the hexagonal opening angle (θ) increases. The data indicate that as θ increases from 45° (A45-5) to 60° (A60-5), the load-carrying capacity improves from 72.14% to 79.41% of the reference beam. This modest increase does not alter the governing Vierendeel mechanism, consistent with the secondary role of the opening angle.

Mechanics-based interpretation using AISC Design Guide 31

The code-based assessment was used to provide a mechanics-based interpretation of the FE results rather than a formal design verification. Three local limit states specified in AISC Design Guide 31 [1] were considered at the peak load of each model: (i) Vierendeel bending of the T-sections, (ii) web-post flexural buckling, and (iii) web-post horizontal shear. The internal shear force and bending moment at the centroid of each opening were extracted from the FE models using force and moment reaction probes on the relevant cross-sectional surfaces. These values, which serve as input demands for the subsequent checks, are listed in Table 5 for the half-span. The openings are numbered from the support toward the midspan, with "Opening 1" located nearest the support. The remaining openings have identical values due to symmetry.

For the Vierendeel bending check, the transfer of the global moment across each opening was represented by an axial force couple developed in the upper and lower T-sections. The magnitude of the axial force in the T-section is given as follows:

$$P_r = \frac{M}{d_{effec}} \tag{1}$$

Here, d_{effec} is the distance between the centroids of T-sections. The global shear induces a secondary moment in each T-section:

$$M_{vr} = V\left(\frac{A_{T-\sec}}{A_n}\right)\left(\frac{e}{2}\right) \tag{2}$$

For the symmetric cross-section considered in this study, the ratio of the T-section area to the net area, $A_{T\text{-}sec}/A_n$, is equal to 0.5. The nominal axial strength ($P_{n,T\text{-}sec}$) and flexural strength ($M_{n,T\text{-}sec}$) of the T-section were determined in accordance with the provisions of AISC 360 [25] Chapter E and Chapter F, respectively. In these calculations, the T-section was treated as the compression element, and the unbraced length was taken as e. Subsequently, the interaction between axial force and bending moment was evaluated using the criteria specified in AISC 360 Section H1.

$$\begin{aligned} &\frac{P_r}{P_{n,T-\sec}} + \frac{8}{9}\frac{M_{vr}}{M_{n,T-\sec}} \le 1.0 \quad \text{for } \frac{P_r}{P_{n,T-\sec}} \ge 0.2 \\ &\frac{1}{2}\frac{P_r}{P_{n,T-\sec}} + \frac{M_{vr}}{M_{n,T-\sec}} \le 1.0 \quad \text{for } \frac{P_r}{P_{n,T-\sec}} < 0.2 \end{aligned} \tag{3}$$

Table 6 presents the maximum interaction ratio observed among all openings, along with the corresponding values of $P_r/P_{n,T\text{-}sec}$ and $M_{vr}/M_{n,T\text{-}sec}$ calculated at the location of the critical opening.

For the web-post checks, the horizontal shear demand between adjacent openings and the associated web-post flexural demand were evaluated using AISC Design Guide 31. The horizontal shear in the web-post between two adjacent openings was computed as:

Table 5. Global shear and bending moment at each opening

	Opening 1		Opening 2		Opening 3		Opening 4	
Beam	V (kN)	M (kNm)	V (kN)	M (kNm)	V (kN)	M (kNm)	V (kN)	M (kNm)
A40-5	294	505	147	649	1	696	-	-
A40-7	377	228	252	434	126	558	1	599
A45-5	279	323	139	491	0	547	-	-
A45-6	297	168	178	358	60	453	-	-
A52-5	266	396	133	538	1	586	-	-
A52-7	296	116	197	292	99	398	1	433
A60-5	242	449	122	564	1	602	-	-
A60-8	299	93	214	256	129	364	43	418
A63-5	242	517	122	623	1	658	-	-
A63-8	354	188	253	364	151	481	51	540

Table 6. Vierendeel bending check at the critical opening

Beam	P_r (kN)	M_{vr} (kNm)	$P_{n,T\text{-}sec}$ (kN)	$M_{n,T\text{-}sec}$ (kNm)	$P_r/P_{n,T\text{-}sec}$	$M_{vr}/M_{n,T\text{-}sec}$	Max. ratio
A40-5	933.5	11.0	997.9	17.8	0.935	0.618	1.486
A40-7	802.8	9.4	997.9	17.8	0.804	0.528	1.276
A45-5	570.8	13.9	948.1	7.9	0.602	1.759	2.165
A45-6	296.3	14.8	948.1	7.9	0.313	1.873	1.978
A52-5	699.8	13.2	948.1	7.9	0.738	1.671	2.233
A52-7	205.9	14.8	948.1	7.9	0.217	1.873	1.878
A60-5	794.1	12.1	948.1	7.9	0.838	1.532	2.195
A60-8	165.0	15.0	948.1	7.9	0.174	1.898	1.977
A63-5	934.1	12.1	981.7	12.4	0.952	0.976	1.820
A63-8	340.2	17.7	981.7	12.4	0.347	1.427	1.617

$$V_{rh} = \frac{\left|M_{(i+1)} - M_{(i)}\right|}{d_{effec}} \tag{4}$$

The required flexural strength was calculated as:

$$M_{rh} = V_{rh}\left(h_0/2\right) \tag{5}$$

The nominal flexural strength M_n was obtained from AISC Design Guide 31 as:

$$M_n = \left(\frac{M_{ocr}}{M_p}\right) M_p \tag{6}$$

Here, M_p is the plastic moment:

$$M_p = 0.25 t_w \left(e + 2b\right)^2 F_y \tag{7}$$

The reduction factor M_{ocr}/M_p was obtained from the design expressions provided in AISC Design Guide 31 for web-post flexural buckling. These expressions are based on the web buckling study of Aglan and Redwood [26] and are given for hexagonal cut angles of 45° and 60°. For each cut angle, separate expressions are provided for e/t_w values of 10, 20, and 30. In the present calculations, linear interpolation was applied between the available e/t_w values and, where applicable, between the 45° and 60° cut-angle expressions. For the 40° and 63° models, which fall outside the calibrated angular range, the nearest available cut-angle expression was adopted.

The nominal horizontal shear capacity was calculated as follows:

$$V_n = 0.6 F_y t_w e \tag{8}$$

The maximum demand-to-capacity ratios across all web posts of each model are reported in Tables 7 and 8.

The ratios presented in Tables 6-8 should be interpreted with caution, as each verification is performed using different demand parameters and definitions of nominal resistance. For instance, the flexural strength of the T-section in the Vierendeel mechanism check is determined using the elastic section modulus ($W_{ex,min}$), which corresponds to a yield-based resistance rather than the fully plastic moment capacity. Also, the AISC 360 Section H1 equation defines a simplified interaction envelope for combined axial and flexural demands. Therefore, these ratios serve as indicators of the relative utilization for each limit state and must be considered alongside the failure modes identified in the finite element analyses.

Table 7. Web-post flexural buckling check

Beam	M_{rh} (kNm)	M_n (kNm)	M_{rh}/M_n
A40-5	39.9	47.3	0.844
A40-7	57.3	47.3	1.211
A45-5	59.4	66.5	0.894
A45-6	67.5	66.5	1.015
A52-5	50.5	68.8	0.735
A52-7	62.2	68.8	0.904
A60-5	40.7	65.0	0.626
A60-8	57.4	65.0	0.883
A63-5	33.4	50.1	0.666
A63-8	55.5	50.1	1.107

Table 8. Web-post horizontal shear check

Beam	V_{rh} (kN)	V_n (kN)	V_{rh}/V_n
A40-5	265.9	255.6	1.040
A40-7	381.9	255.6	1.494
A45-5	296.8	340.8	0.871
A45-6	337.0	340.8	0.989
A52-5	252.4	340.8	0.741
A52-7	311.0	340.8	0.913
A60-5	203.6	340.8	0.597
A60-8	286.9	340.8	0.842
A63-5	190.7	340.8	0.560
A63-8	317.1	340.8	0.930

The Vierendeel interaction ratio is closely related to the geometric ratio $2d_t/d_g$. The ratio is 1.38 for $2d_t/d_g$=0.50, 1.72 for $2d_t/d_g$=0.42, and 2.07 for $2d_t/d_g$=0.33. This indicates that Vierendeel demand becomes more critical as the T-sections become shallower. This trend is mainly associated with the reduction in T-section flexural strength, since $M_{n,T\text{-}sec}$ decreases from 17.8 to 12.4 and 7.9 kNm as d_t decreases from 150 to 125 and 100 mm, while $P_{n,T\text{-}sec}$ remains nearly constant.

Mechanically, $M_{n,T\text{-}sec}$ is governed by the elastic section modulus $W_{ex,min}$. As shown in Table 9, $W_{ex,min}/d_t^2$ remains nearly constant within the investigated range, indicating that the T-section modulus varies approximately with d_t^2.

Therefore, reducing $2d_t/d_g$ substantially decreases the resistance to the secondary Vierendeel moment and promotes plastic hinge formation around the openings.

Table 9. Elastic section modulus ($W_{ex,min}$), nominal flexural strength ($M_{n,T\text{-}sec}$), and the ratio $W_{ex,min}/d_t^2$ of the T-section for the three depths.

d_t (mm)	$W_{ex,min}$ (mm³)	$M_{n,T\text{-}sec}$ (kNm)	$W_{ex,min}/d_t^2$ (mm)
150	50131	17.8	2.228
125	34895	12.4	2.233
100	22308	7.9	2.231

Table 6 further clarifies the transition at the T-section level. For $2d_t/d_g$=0.50, the interaction is mainly associated with axial force, while the Vierendeel moment remains within the T-section capacity. In contrast, for $2d_t/d_g$=0.33, Vierendeel bending becomes dominant, with $M_{vr}/M_{n,T\text{-}sec}$ values between 1.53 and 1.90. The intermediate case, $2d_t/d_g$=0.42, shows a more balanced axial-bending interaction. These trends show that reducing $2d_t/d_g$ shifts the response toward local Vierendeel bending, whereas higher ratios help maintain a global flexural response.

The results of the Vierendeel check indicate that the opening angle has a secondary influence within this subset of models. For models with $2d_t/d_g$=0.33 and five openings, the Vierendeel ratios remain relatively close, with values of 2.165, 2.233, and 2.195 for A45-5, A52-5, and A60-5, respectively. This trend suggests that, when the T-section depth and number of openings are comparable, the opening angle alone is not a sufficient predictor of structural performance. This interpretation is consistent with previous studies by Budi et al. [7] and Barkiah and Darmawan [9], which reported different optimum opening angles.

The web-post checks in Tables 7 and 8 show higher web-post utilization in the models with more openings. In the simply supported configuration considered here, a larger number of openings places some openings closer to the supports, where the shear force is higher. The resulting increase in the local shear and moment demands on the web post, rather than the number of openings in itself, is responsible for the higher web-post utilization. The most critical case is A40-7, with a web-post horizontal shear ratio of 1.49 and a web-post flexural buckling ratio of 1.21, despite having the lowest Vierendeel interaction ratio due to its deep T-section. This agrees with the FE results, where plastic strain was concentrated in the horizontal web-post region and the load-displacement response did not develop a well-defined post-peak plateau. Therefore, in A40-7, the critical region shifts from the T-sections to the web post.

Overall, the design-code checks support the failure-mode interpretation obtained from the FE analyses. The Vierendeel check highlights the role of $2d_t/d_g$ in the transition from global flexural behavior to local Vierendeel mechanisms, whereas the web-post checks show that the web-post region can become critical when openings are positioned closer to the supports. Therefore, $2d_t/d_g$ is a useful indicator of the flexural-to-Vierendeel transition, but the position of the openings relative to the high-shear regions should also be considered.

Conclusion

A nonlinear FE analysis was conducted to investigate the influence of geometric parameters of hexagonal web openings on the failure modes of constant-depth perforated steel beams. Ten perforated beam models were systematically compared with a solid-web reference beam. The principal findings are summarized as follows.

1. Two primary failure types were observed in the perforated beams. The first was a ductile, high-capacity response characterized by the formation of a flexural plastic hinge at mid-span, as observed in models A40-5 and A63-5. The second was a brittle, low-capacity response governed by a shear-related mechanism (Vierendeel bending or web-post buckling) localized around the web openings near the supports.

2. The most consistent geometric indicator of the failure-mode transition in the investigated models was the dimensionless ratio of the total T-section depth to the overall beam depth ($2d_t/d_g$). Models exhibiting ductile flexural failure had the highest $2d_t/d_g$ ratios (0.50 and 0.42), whereas models with a lower $2d_t/d_g$ ratio (0.33) failed in a brittle Vierendeel mode. The design-code evaluation based on AISC Design Guide 31 supported this trend by relating it to the T-section flexural capacity, which decreases approximately with the square of the T-section depth and therefore reduces the resistance to the Vierendeel moment.

3. The opening angle (θ) had a secondary influence within the investigated range. For beams with a low $2d_t/d_g$ ratio of 0.33, increasing the opening angle from 45° to 60° (corresponding to a decrease in the b/h_o ratio) resulted in only a modest increase in capacity from 72.1% to 79.4%. However, this adjustment did not prevent the occurrence of the undesirable Vierendeel failure mode.

4. The location of the openings relative to the shear-force distribution had an important influence on the structural response. In the simply supported beam configuration considered in this study, increasing the number of openings placed some openings closer to the supports, where the shear force is higher. As a result, shear-related mechanisms, such as Vierendeel bending and web-post shear/buckling, became more pronounced. This behavior was particularly evident in models such as A40-7 and A60-8, where the critical response was associated with openings located in higher-shear regions rather than with the number of openings alone.

5. The results suggest that considering only the opening angle (θ) is insufficient for the design of perforated beams. The relatively high capacity of the A40-5 model is associated with its larger $2d_t/d_g$ ratio rather than with the 40° opening angle alone. For the investigated beam configuration, increasing the $2d_t/d_g$ ratio appears beneficial for promoting ductile flexural behavior instead of brittle shear failure at the web openings.

6. Within the five-opening model series, a $2d_t/d_g$ ratio of approximately 0.42 or higher promoted ductile flexural behavior, whereas a ratio of 0.33 resulted in brittle Vierendeel failure. However, this value should be interpreted as a preliminary reference for comparable constant-depth perforated beams with similar web-post proportions and similar opening locations relative to the shear-force distribution. When additional openings are placed closer to the supports, shear-related demand may become more critical and shift the governing response toward Vierendeel bending or web-post shear/buckling.

These findings apply to the investigated beam depth, the S355 material grade, and the modeling assumptions adopted in this study, particularly the restraint of lateral-torsional buckling. Therefore, the results should be interpreted within these limits.

Future research should include experimental validation of these numerical findings and further investigation of the effects of lateral-torsional buckling. The influence of residual stresses, initial geometric imperfections, and alternative opening configurations should also be examined in future studies.

Ethics committee approval and conflict of interest statement

There is no need to obtain permission from the ethics committee for the article prepared.

There is no conflict of interest with any person / institution in the article prepared.

Authors' Contributions

-Study conception and design: OY

-Acquisition of data: OY, YEÖ

-Analysis and interpretation of data: OY, YEÖ

-Drafting of manuscript: OY, YEÖ

-Critical revision: OY

References

[1] *Design Guide 31: Castellated and Cellular Beam Design*, AISC, Chicago, IL, USA, 2017.

[2] D. Kerdal, and D. A. Nethercot, "Failure modes for castellated beams," *J. Constr. Steel Res.*, vol. 4, no. 4, pp. 295-315, 1984, DOI: 10.1016/0143-974X(84)90004-X

[3] R. Deepha, and S. Jayalekshmi, "Finite element analysis on shear strength of a castellated beam with hexagonal web opening", *IOP Conf. Ser.: Mater. Sci. Eng.*, vol. 1006, no. 1, 2020, Art. no. 012009, DOI: 10.1088/1757-899X/1006/1/012009

[4] W. Zaarour, and R. Redwood, "Web buckling in thin webbed castellated beams," *J. Struct. Eng.*, vol. 122, no. 8, pp. 860-866, 1996, DOI: 10.1061/(ASCE)0733-9445(1996)122:8(860)

[5] R. Redwood, and S. Demirdjian, "Castellated beam web buckling in shear," *J. Struct. Eng.*, vol. 124, no. 10, pp. 1202-1207, 1998, DOI: 10.1061/(ASCE)0733-9445(1998)124:10(1202)

[6] K. D. Tsavdaridis, and C. D'Mello, "Vierendeel bending study of perforated steel beams with various novel web opening shapes through nonlinear finite-element analyses," *J. Struct. Eng.*, vol. 138, no. 10, pp. 1214-1230, 2012, DOI: 10.1061/(ASCE)ST.1943-541X.0000562

[7] L. Budi, and W. Partono, "Optimization analysis of size and distance of hexagonal hole in castellated steel beams," *Procedia Eng.*, vol. 171, pp. 1092-1099, 2017, DOI: 10.1016/j.proeng.2017.01.465

[8] P. Ponsorn, and K. Phuvoravan, "Efficiency of castellated and cellular beam utilization based on design guidelines," *Pract. Period. Struct. Des. Constr.*, vol. 25, no. 3, 2020, Art. no. 04020016, DOI: 10.1061/(ASCE)SC.1943-5576.000049

[9] L. Barkiah, and A. R. Darmawan, "Comparative analysis of the flexural capacity of conventional steel beams with castellated beams," *IOP Conf. Ser.: Earth Environ. Sci.*, vol. 780, no. 1, 2021, Art. no. 012013, DOI: 10.1088/1755-1315/780/1/012013

[10] F. P. V. Ferreira, R. Shamass, L. F. P. Santos, V. Limbachiya, and K. D. Tsavdaridis, "EC3 design of web-post buckling resistance for perforated steel beams with elliptically-based web openings," *Thin-Walled Struct.*, vol. 175, 2022, Art. no. 109196, DOI: 10.1016/j.tws.2022.109196

[11] S. G. Morkhade, and L. M. Gupta, "Critical study of steel beams with web openings," *Aust. J. Struct. Eng.*, vol. 24, no. 1, pp. 24-35, 2023, DOI: 10.1080/13287982.2022.2117319

[12] S. G. Morkhade, L. M. Gupta, and C. H. Martins, "Effect of Web Post Width on Strength Capacity of Steel Beams with Web Openings: Experimental and Analytical Investigation," *Pract. Period. Struct. Des. Constr.*, vol. 27, no. 2, 2022, Art. no. 04022010, DOI: 10.1061/(ASCE)SC.1943-5576.0000688

[13] A. Khan, C. H. Martins, A. Rossi, and S. G. Morkhade, "Evaluation of web post-buckling and vierendeel mechanism in steel alveolar beams with five shapes of web openings: a numerical study," *J. Build. Pathol. Rehabil.*, vol. 11, Art. no. 118, 2026, DOI: 10.1007/s41024-026-00800-2

[14] S. S. Patil, and P. D. Kumbhar, "Comparative study on the behaviour of castellated beams provided with

hexagonal, circular, and diamond-shaped web openings," *Asian J. Civ. Eng.*, vol. 25, pp. 359-369, 2024, DOI: 10.1007/s42107-023-00780-5

[15] F. De'nan, C. S. Wai, and N. S. Hashim, "Impact of web perforation size and shapes on structural behavior: a finite element analysis," *World J. Eng.*, vol. 21, no. 5, pp. 911-923, 2024, DOI: 10.1108/WJE-03-2023-0076

[16] N. S. Hashim, and F. De'nan, "The numerical assessment of stress distribution of I-beam with web opening," *World J. Eng.*, vol. 21, no. 5, pp. 986-1001, 2024, DOI: 10.1108/WJE-03-2023-0078

[17] G. Promsatit, T. Sethaput, W. Atjanakul, and A. Boonyaprapasorn, "Enhancing web-post buckling resistance in perforated steel beams: An in-depth investigation of elliptical openings, geometric parameters, and ai-driven predictions," *Structures*, vol. 71, 2025, Art. no. 107907, DOI: 10.1016/j.istruc.2024.107907

[18] W. Sae-Long, S. Arun, S. Limkatanyu, P. Chaimahawan, N. Damrongwiriyanupap, W. Fakkaew, and S. Wongchairattana, "Behavior and design implications of web-post shear failure in cellular beams," *Results Eng.*, vol. 27, 2025, Art. no. 106709, DOI: 10.1016/j.rineng.2025.106709

[19] W. Sae-Long, S. Arun, A. Witthayapraphakorn, S. Limkatanyu, N. Damrongwiriyanupap, W. Fakkaew, P. Chaimahawan, and C. Thongchom, "Local failure behavior of cellular beams: A parametric finite element study of web-post bending moment," *Results Eng.*, vol. 29, 2026, Art. no. 109372, DOI: 10.1016/j.rineng.2026.109372

[20] J. Betken, A.-L. Bours, R. Winkler, and M. Knobloch, "Numerical analysis of the stability behaviour of castellated beams and comparison to regular hot-rolled profiles," *Steel Constr.*, vol. 19, no. 1, pp. 50-59, 2026, DOI: 10.1002/stco.70007

[21] P. K. Bhat, S. Ashwitha, and D. K. Bhat, "Span-dependent comparative analysis of lateral torsional buckling and nonlinear load behaviour in castellated and solid I-beams using analytical and finite element approaches," *Mater. Res. Express,* vol. 12, 2025, Art. no. 125701, DOI: 10.1088/2053-1591/ae284c

[22] Ansys® Academic Research Mechanical, Release 2024 R2, ANSYS, Inc.

[23] K. D. Tsavdaridis, and C. D'Mello, "Web buckling study of the behaviour and strength of perforated steel beams with different novel web opening shapes," *J. Constr. Steel Res.*, vol. 67, no. 10, pp. 1605-1620, 2011, DOI: 10.1016/j.jcsr.2011.04.004

[24] Ansys® Academic Research Mechanical, Release 2024 R2, Help System, Element Reference, ANSYS, Inc.

[25] American Institute of Steel Construction, "Specification for Structural Steel Buildings (ANSI/AISC 360-22)", AISC, Chicago, IL, 2022

[26] A. A. Aglan and R. G. Redwood, "Web buckling in castellated beams," *Proc. Inst. Civ. Eng.*, vol. 52, no. 2, pp. 307-320, 1974, DOI: 10.1680/iicep.1974.4059